PAPER • OPEN ACCESS

ETG turbulent transport in the Mega Ampere Spherical Tokamak (MAST) pedestal

To cite this article: P.-Y. Li *et al* 2024 *Nucl. Fusion* **64** 016040

OPEN ACCESS
IOP Publishing | International Atomic Energy Agency
Nuclear Fusion
Nucl. Fusion **64** (2024) 016040 (17pp)
https://doi.org/10.1088/1741-4326/ad0ef9

ETG turbulent transport in the Mega Ampere Spherical Tokamak (MAST) pedestal

P.-Y. Li[1,*], D.R. Hatch[1], B. Chapman-Oplopoiou[2], S. Saarelma[2], C.M. Roach[2], M. Kotschenreuther[1], S.M. Mahajan[1], G. Merlo[1] and the MAST Team

[1] Institution for Fusion Studies, The University of Texas at Austin, Austin, TX, United States of America
[2] UKAEA CCFE, Culham Science Centre, Abingdon, Oxon, United Kingdom of Great Britain and Northern Ireland

E-mail: pingyu.li@austin.utexas.edu

Received 30 August 2023, revised 1 November 2023
Accepted for publication 22 November 2023
Published 8 December 2023

Abstract

The results of a gyrokinetic analysis of turbulent transport driven by the electron temperature gradient (ETG) in the MAST pedestal are presented. Local nonlinear simulations from the gyrokinetic code, GENE, show that heat flux produced by ETG turbulence is 10%–30% of the total applied heating power in the upper pedestal and pedestal top during both the pre-edge-localized mode (ELM) (80%–99% inter-ELM period) and post-ELM (0%–20%) periods. Increasing strongly with the ETG, the ETG transport appears to be stiff. Considering radiation losses, ion thermal transport, and the strong sensitivity of the transport to the ETG, we propose that ETG transport is a plausible mechanism mediating the inter-ELM temperature profile on MAST. Cognizant of the possibility that sharp variations in the pedestal profiles may violate the local approximation, we conducted global nonlinear simulations; the results are in good agreement with local simulations except near the pedestal top, where extended radial structures and high transport levels (far beyond experimental) develop in the local simulations. We quantify and parameterize the discrepancy between local and global simulations by calculating the ratio of the radial correlation length to a length scale representative of the profile curvature. When this ratio is sufficiently small, local and global simulations agree as expected.

Keywords: ETG, MAST, nonlocal effects, pre-ELM and post-ELM

(Some figures may appear in colour only in the online journal)

1. Introduction

In tokamaks, including the Mega Ampere Spherical Tokamak (MAST), a narrow transport barrier that improves the confinement of magnetized plasma is formed in the high confinement mode (H mode) [1]. This barrier supports high density and temperature gradients at the edge of the plasma, which leads to the development of a steep pressure pedestal. In MAST, this pedestal undergoes a cyclical process of growth and collapse by an edge-localized mode (ELM) [2]. During this process, the electron density pedestal builds up much faster than the electron temperature pedestal, suggesting that an electron thermal transport mechanism may be active and constraining the inter-ELM pedestal evolution. This paper uses the gyrokinetic code, GENE [3, 4], to investigate the role of electron temperature gradient (ETG) driven turbulent transport in the MAST pedestal.

* Author to whom any correspondence should be addressed.

Historically, it was believed that ETG turbulence would not significantly affect transport due to low transport levels predicted by simple mixing length estimates. However, nonlinear gyrokinetic simulations have shown that the formation of radially-extended structures, also known as streamers, in the nonlinear turbulent state can potentially lead to significant ETG transport in conventional tokamaks [3, 5, 6]. Recent work has determined that ETG can produce substantial transport in the pedestal [7–20]. Typically the ETG transport in the pedestal does not rely on streamers. Rather, the fluctuations remain relatively isotropic [9, 21] and achieve substantial heat fluxes due to the extreme pedestal gradients.

This paper presents linear and nonlinear, local and global gyrokinetic analyses of ETG in the MAST pedestal. Simulations produce ETG turbulence at experimentally-relevant transport levels with transport increasing rapidly with $\eta = L_n/L_T$ (i.e. the transport is stiff), where $L_{n,T}$ are the electron density and temperature gradient scale lengths, respectively. This is the case during both pre-ELM (80%–99% inter-ELM period) and post-ELM (0%–20%) periods in the density pedestal top (the flat region above the pedestal) and upper pedestal region (the transition part from steep gradient region to pedestal top), which will be discussed in sections 2 and 3, respectively. We conclude that ETG turbulence likely plays a significant role in electron thermal transport in the MAST pedestal. This ETG transport likely acts together with microtearing modes (MTMs), which have been studied previously [22], to constrain the electron temperature pedestal, while pressure gradient is constrained by KBM and the total pedestal pressure is limited by the ideal MHD peeling-ballooning modes [22, 23]. The combination of ETG and MTM has also been identified in standard aspect ratio pedestals [10, 12, 24–26].

Since ETG fluctuates at such small scales, a local approximation is typically thought to be adequate even for the exceptionally steep gradients in the pedestal (although the need for a global treatment of streamers has been discussed in [27, 28]). We explicitly investigate nonlocal effects by comparing local and global nonlinear simulations. This comparison is particularly relevant for the MAST pedestal due to its comparatively weak magnetic field (compared to comparable standard aspect ratio tokamaks), which results in weaker scale separation between gyro-radius scales and equilibrium scales. We find close agreement at most locations, but substantial deviation in the region where the density profile transitions from the pedestal to the core (i.e. where profile curvature, defined as the first order term of the expansion $\frac{\nabla n}{n}(x)$ or $\frac{\nabla T}{T}(x)$), is large). In this region, local simulations produce anomalously large transport levels. In contrast, global simulations produce much lower transport levels. These findings provide insight into the mechanisms behind the formation of the pedestal, which may enable improved confinement in spherical tokamaks.

The presentation of the results is organized as follows: in section 2, we demonstrate the activity of ETG turbulence based on local linear and nonlinear pre-ELM simulations. Sensitivity tests for linear and nonlinear gyrokinetic simulations are conducted by varying the density and temperature gradients, and global nonlinear gyrokinetic simulations are compared to local simulations at different radial locations. This section illustrates that ETG turbulence is sensitive to gradients and can be affected by global effects. Local post-ELM simulations are presented in section 3 and compared to pre-ELM simulations, revealing the continued activity of ETG turbulence across the inter-ELM period. We also study energy triplet diagnostics and energy transfers across scales to demonstrate that ETG turbulence is saturated by forward cascade accompanied by some backward cascade in MAST. Further details on this are discussed in appendix A. The simulation setups for the nonlinear simulations will be presented in appendix B.

2. Local pre-ELM simulations

In order to check whether ETG turbulence is important in the pedestal, we begin by looking at the region around the pedestal top where $\eta = L_\mathrm{n}/L_\mathrm{T}$, the ratio of density scale length and temperature scale length, is large.

As shown in figures 1 and 2, three radial locations at $\rho_\mathrm{tor} = 0.92, 0.94, 0.96$ are picked to cover the pedestal top for the test during the pre-ELM stage. Note that $f_p = \omega_n/(\omega_n + \omega_T)$ is used to quantify the portion of the free energy available from density gradient that drives instability, where normalized density gradient $\omega_{\mathrm{n_e}} = \omega_{\mathrm{n_i}} = \omega_\mathrm{n} = a/L_\mathrm{n}$, and normalized temperature gradient $\omega_\mathrm{Te} = \omega_\mathrm{Ti} = \omega_\mathrm{T} = a/L_\mathrm{T}$. We focus particularly on this upper pedestal region since transport is found to be low from ETG at $\rho_\mathrm{tor} = 0.96$ already as shown later, the steep gradient region with even smaller η and T_ref is therefore not a region of interest for ETG transport.

ρ_tor is the square root of normalized toroidal flux. Table 1 shows the physical input parameters for the simulations where the normalized plasma pressure $\beta = 8\pi n_{\mathrm{e}0} T_\mathrm{ref}/B^2_\mathrm{ref}$, the safety factor q_0, the normalized magnetic shear $\hat{s} = \frac{r}{q}\frac{\mathrm{d}q}{\mathrm{d}r}$ with r as the flux surface label, reference magnetic field in Tesla B_ref, reference temperature in keV T_ref, reference density in $10^{19} m^{-3}$, and the ratio ion gyroradius and minor radius $\rho^* = \rho_\mathrm{i}/a$. Also note that a and R are the minor and major radii, respectively, the effective ion charge Z_eff is set to 2 for the collision operator, and the ion and electron temperatures and densities are set equal for all simulations.

Figure 3 shows the growth rate spectrum, growth rate γ versus binormal wavenumber $k_y\rho_s$, calculated at different radial locations with linear gyrokinetic initial value runs centered at the outboard mid-plane, where ρ_s is the ion gyroradius and c_s is the ion sound speed. Note that $\hat{e}^x$, $\hat{e}^y$, and $\hat{e}^z$ are radial, binormal, and tangent unit vector in GENE convention, respectively.

Table 2 shows some of the important characteristic values of the most unstable modes (electron scales) at three radial locations used to categorize the instabilities. In this table, ω is the real frequency, χ is the heat diffusivity, and D_e is the particle diffusivity. These instabilities are highly electrostatic electron waves with low particle flux, which of course can be identified as ETG modes [13]. One interesting observation from figure 3 is that the peak of the growth rate spectrum moves to smaller scales as the radial location moves outward. A simple mixing

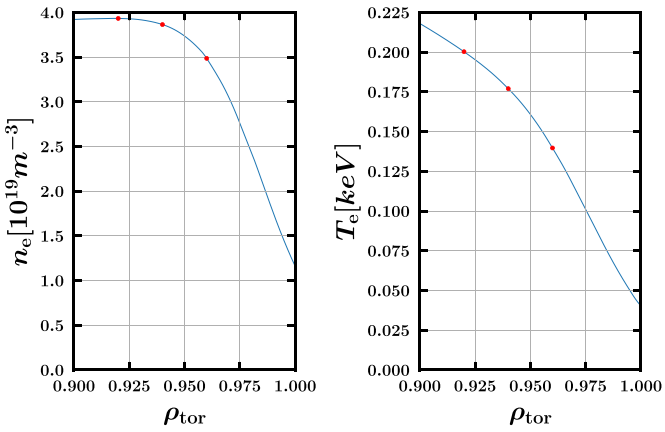

Figure 1. The electron density and temperature versus the square root of the normalized toroidal flux surface label ρ_{tor} during pre-ELM stage.

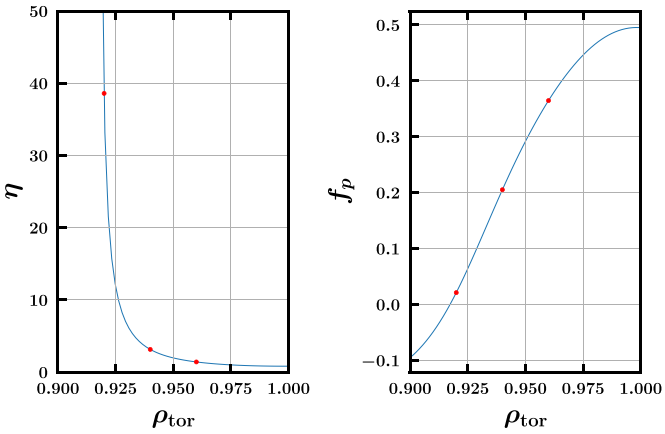

Figure 2. η and f_p versus the normalized toroidal flux surface label ρ_{tor} during pre-ELM stage. η is 38.6, 3.79, and 1.72 for $\rho_{tor} = 0.92$, 0.94, and 0.96, respectively. $f_p = \frac{a/L_n}{a/L_n + a/L_T}$ is used to quantify the portion of the free energy contributed by the temperature gradient, the closer it is to 0.6, the less likely the temperature-gradient-driven instability can access the free energy from temperature gradient [29].

Table 1. The physical input parameters at $\rho_{tor} = 0.92, 0.94, 0.96$, respectively. η and β decrease as ρ_{tor} increases. Magnetic shear does not vary a lot around the pedestal top.

ρ_{tor}	q_0	$\hat{s}$	ω_n	ω_T	η	β	B_{ref}	T_{ref}	n_{ref}	ρ^*
0.92	5.41	4.16	0.126	4.86	38.6	0.0136	0.483	0.200	3.93	0.004 99
0.94	5.92	4.14	2.16	8.13	3.79	0.0118	0.483	0.177	3.86	0.004 69
0.96	6.46	4.20	9.71	16.7	1.72	0.0084	0.483	0.140	3.48	0.004 16

length estimate (not shown), $\chi \sim \gamma/k_y^2$, would predict that the thermal diffusivity would decrease as the radial location increases (for example, note that the peak k_y approximately doubles as does the peak growth rate comparing $\rho_{tor} = 0.92$ and $\rho_{tor} = 0.96$). Moreover, the gyroBohm prefactor decreases strongly as temperature and density decrease across the pedestal. This quick assessment predicts that ETG heat fluxes decrease substantially at larger radial positions in the pedestal, which is confirmed by the nonlinear simulations described below with the numerical info included in appendix B.

Figure 4 shows the heat fluxes derived from local nonlinear gyrokinetic simulations at three different radial locations in megawatts (MW). The simulations include $E \times B$ shear and $k_{ymin}\rho_s$ is set as 6. The heat flux is calculated to be 14.48 MW at $\rho_{tor} = 0.92$, which is far higher than the heat fluxes 0.38 MW and 0.08 MW calculated at $\rho_{tor} = 0.94$ and 0.96, respectively. This discharge is heated by NBI at a level of 3.2 MW. Although a detailed analysis is not available, some fraction of the heating power is lost as radiation, some fraction is also transported through the ion channel, and some of the energy is transported when the pedestal collapses in ELMs. We will proceed by assuming that something on the order of 1 MW is a plausible expectation for electron thermal transport. Note that the evolution of the temperature profile is quite slow in the pre-ELM period, but it is not in a fully steady state between ELMs (see, e.g. [22]). Based on this assumption, only the result at $\rho_{tor} = 0.94$ is in the proximity of experimental expectations. However, we as will be shown below,

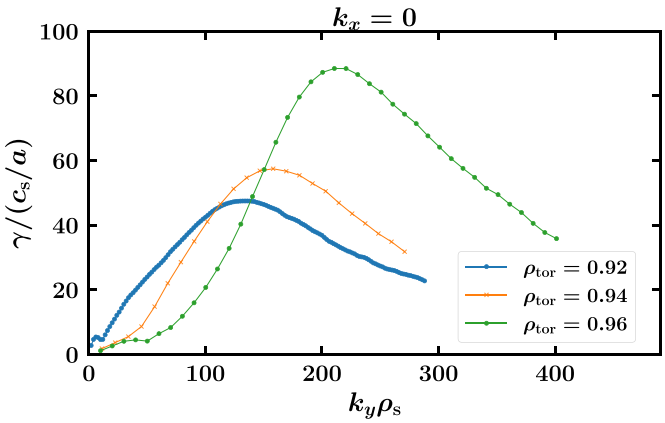

Figure 3. Growth rate spectrum γ versus $k_y\rho_s$ during pre-ELM stage with c_s and ρ_s calculated at $\rho_{tor} = 0.92$. Growth rate spectrum peaks at a smaller scale for the outer radial location for similar k_x, implying the heat flux can be smaller for larger ρ_{tor} based on simple mixing length estimates.

Table 2. Characteristic values for the most unstable mode at three different radial locations. Low χ_{em}/χ_{es}, low χ_i/χ_e, and small D_e/χ_e imply that these instabilities are electrostatic, electron dominant, and have low particle flux, respectively. Therefore, these instabilities are ETG modes.

ρ_{tor}	$k_y\rho_s$	$\gamma(c_s/a)$	$\omega(c_s/a)$	χ_{em}/χ_{es}	χ_i/χ_e	D_e/χ_e
0.92	136	47.5	−137.1	-1.24×10^{-3}	1.27×10^{-3}	−0.161
0.94	168	60.4	−134.8	-1.06×10^{-3}	1.07×10^{-2}	-7.5×10^{-3}
0.96	252	105.9	−144.5	4.62×10^{-4}	2.36×10^{-2}	5.12×10^{-3}

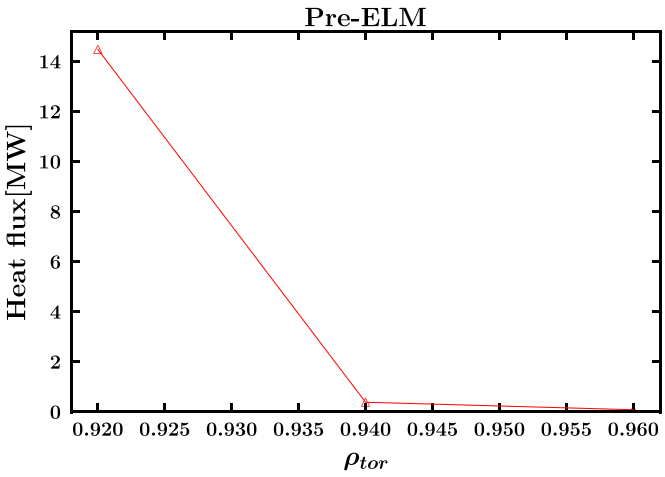

Figure 4. Heat fluxes calculated at $\rho_{tor} = 0.92, 0.94$, and 0.96 are 14.48, 0.38, and 0.08 MW, respectively. With regard to the 3.2 MW NBI power of MAST, the local nonlinear simulation predicts inaccurate heat flux, global effects need to considered.

all three radial positions plausibly produce reasonable transport levels when global effects and/or parameter sensitivities are considered. More specifically, global effects decrease the transport substantially at $\rho_{tor} = 0.92$. Moreover, the transport at $\rho_{tor} = 0.92, 0.94$ is found to be in experimentally-realistic ranges when density and temperature gradients are slightly modified.

Due to the typical extreme sensitivity of turbulent transport to gradients, a thorough investigation must probe experimental uncertainties in the profiles. The profiles used for the simulations averaged over several ELM cycles. Although rigorous uncertainties are difficult to quantify, the error bar of the gradients can exceed 20%. It is then reasonable to vary the gradients within this range in order to check what is the highest heat flux the instabilities can produce and how stiff the transport is.

Figure 5 shows how the growth rate spectrum changes when the density and temperature gradients are varied at $\rho_{tor} = 0.94$ during the pre-ELM stage. When the temperature gradient a/L_{T0} is increased by 20%, the growth rates at all scales are also increased by approximately 20%. Note that it is also observed in other machines such as NSTX [7], DIII-D [16], JET [30], etc, that ETG turbulence is sensitive to temperature gradient. The temperature gradient sensitivity The On the

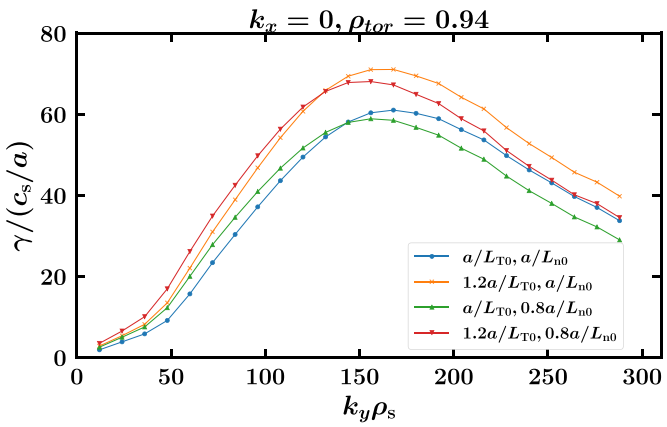

Figure 5. Growth rate spectrum at $\rho_{\rm tor} = 0.94$ during the pre-ELM stage. The spectrum is moved upward about 20% when the temperature gradient $a/L_{\rm T0}$ is increased by 20%, and moved horizontally toward the larger scale when $a/L_{\rm n0}$ s decreased.

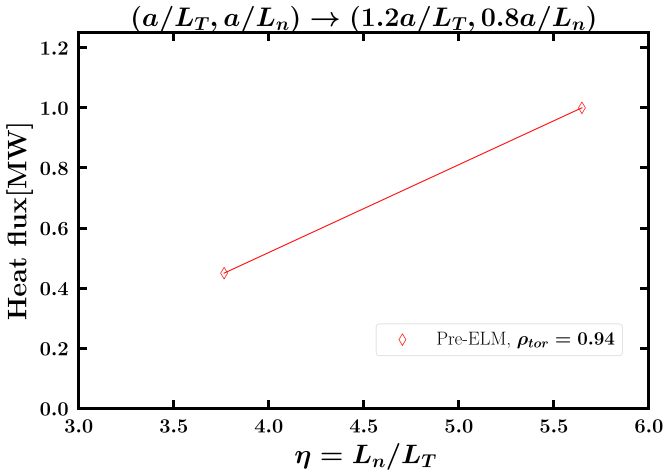

Figure 6. Heat fluxes calculated at $\rho_{\rm tor} = 0.94$ for the pre-ELM stage shows the heat flux increased significantly when there is a 20% increase in $a/L_{\rm T0}$ and a 20% decrease in $a/L_{\rm n0}$. The amount of heat flux increased is more profound than the result got from linear simulations.

other hand, when the density gradient $a/L_{\rm n0}$ is decreased by 20%, the growth rate spectrum is not shifted upward, instead, it is shifted toward the larger scales. The case with 20% increase in $a/L_{\rm T0}$ and 20% decrease in $a/L_{\rm n0}$ increases the growth rates preferentially at low k_y, which are the most important modes for transport, by up to 40%. This result suggests ETG turbulence does not depend solely on $\eta = L_{\rm n}/L_{\rm T}$, its growth rate is more responsive to the change of the temperature gradient. The heat fluxes obtained from nonlinear local gyrokinetic simulations in the pre-ELM stage at radial locations of $\rho_{\rm tor} = 0.94$ is shown in figure 6. The simulations reveal that the heat flux increases significantly when there is a 20% increase in $a/L_{\rm T0}$ and a 20% decrease in $a/L_{\rm n0}$. Specifically, the pre-ELM case shows a 110% increase in heat flux. We note that this increase is much higher than the corresponding increase in the maximum growth rates, which exhibit an increase of only ∼40%. The results suggest that ETG turbulence is highly sensitive to the gradients, and even a slight increase in the pedestal temperature gradient can lead to significant heat flux changes. These results also highlight the importance of investigating how ETG turbulence in the pedestal top for spherical tokamaks saturates, and suggests that deeper investigation into the nonlinear effects is needed.

2.1. Nonlocal effects

We return now to the exceptionally high heat flux predicted at $\rho_{\rm tor} = 0.92$ (see figure 4), which far exceeds the total heating power for this discharge. The growth rates at the lower k_y wavenumbers, shown in figure 3, significantly surpass those at $\rho_{\rm tor} = 0.94$ and 0.96. Even so, the unrealistically large heat flux is not expected from simple mixing length estimates derived from the growth rate spectrum.

The results presented in figure 7 illustrate a comparative analysis between calculated global and local heat fluxes including an additional local simulation conducted at $\rho_{\rm tor}$= 0.93. In this context, the parameter *ck* denotes the krook type heat source in time units of $c_{\rm ref}/L_{\rm ref}$, where a value of $ck = 5$ is chosen to maintain minimal alterations in the temperature profile. Notably, simulations employing higher values

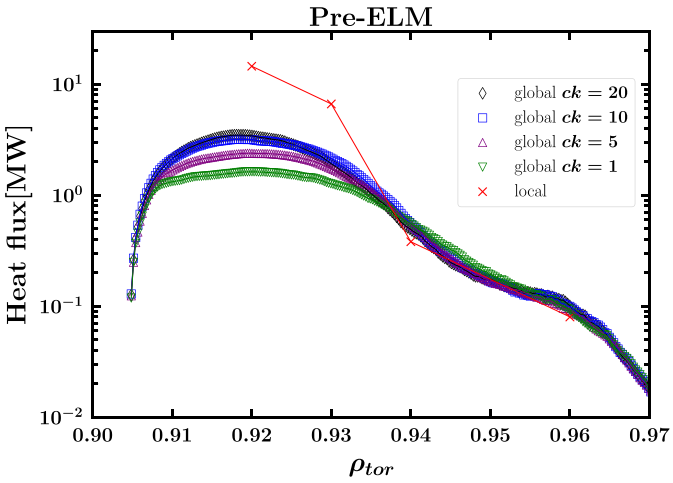

Figure 7. The heat flux radial profile calculated from a global nonlinear simulation during the pre-ELM period, comparing with results from local nonlinear simulations at $\rho_{\rm tor} = 0.92$, 0.93, 0.94, and 0.96. Where ck represents the heat source in unit of $c_{\rm ref}/L_{\rm ref}$, with $ck = 5$ keeping the temperature profile nearly unchanged. The heat fluxes calculated at $\rho_{\rm tor} = 0.94$ and 0.96 agree with the result derived from global simulation with minor differences while those at $\rho_{\rm tor} = 0.92$ and 0.93 are way off, implying that the global effects can be crucial.

of ck, specifically $ck = 10$ and $ck = 20$, introduce excessive energy injection, thereby inducing more pronounced temperature gradients and heightened heat flux in the pedestal top in comparison to the $ck = 5$ scenario. Conversely, the case of $ck = 1$ exhibits a modest relaxation in the pedestal top, leading to reduced temperature gradient and heat flux.

Despite the fact that η and f_p vary enormously over the region $\rho_{\rm tor} = 0.91$–0.93 (recall figure 1), the heat flux profile in the global simulations is comparatively flat. To elucidate, we observe that the profile of the diamagnetic drift ω_{*s} which is proportional to $a/L_n + (v_\parallel^2 + \mu B - 1.5)a/L_T$, varies relatively little in this region where the density profile is flat (i.e. density gradient is vanishingly small) and the temperature gradient is relatively constant (see figure 1) despite η shows strong variations due to small a/L_n. This implies the availability of free energy remains approximately unchanged, and η is a less relevant instability parameter in the pedestal top. Consequently, despite the huge variation in η, the ETG transport remains relatively constant in the pedestal top region. Also note that, since both density and temperature gradients are weaker, ω_{*s} is much smaller than in the steep gradient region and toroidal resonances (i.e. resonances with the magnetic drifts) are possible. Moreover, it will be shown in the next subsection that the transport is sensitive to $E \times B$ shear. The above observations imply ETGs in the pedestal top are most likely toroidal ETGs, which are also known to be much less sensitive to η.

Notably, while the heat fluxes at $\rho_{\rm tor} = 0.94$ and 0.96 agree with the result obtained from the global simulations, with minor differences, those at $\rho_{\rm tor} = 0.92$ and 0.93, with $Q_{es} =$ 14.48 and 6.62 MW, respectively, are far off. The heat fluxes calculated from global simulations at $\rho_{\rm tor} = 0.92$ and 0.93, with 2.38 and 1.74 MW for $ck = 5$, respectively, are much lower, indicating that global effects significantly reduce the heat flux at these locations.

Global and local simulations differ in terms of whether they incorporate the radial variation of profiles and equilibrium. Additionally, it is important to highlight that the boundary conditions employed in local and global simulations are different. Local simulations utilize radially periodic boundary conditions, while global simulations in GENE utilize a Dirichlet boundary condition at both ends of the box. To assess the impact of radially boundary conditions on heat flux transport at the top of the pedestal, the convergence check completed involves modifying the box size, effectively ruling out the influence of boundary conditions. In order to assess the importance of global effects from the radial variation of the profiles, it is necessary to examine the radial structure of turbulence in the local simulation. Here, we present the results of local nonlinear simulations during the saturated state, where the box size L_x is set to $27\rho_s$. Note that to saturate the turbulence, $L_x = 13.5\rho_s$ is shown to be sufficient in the convergence test. Since $\rho^*_{\rm ref} = \rho_s/a = 0.00499$, the equivalent box size as a fraction of the minor radius a is 0.136, which is substantially larger than the entire pedestal (recall figure 1). Figure 8 shows the time slice of the Φ contour plot in real space. The extended structure seen in the figure, combined with the fact that the simulation is located at $\rho_{\rm tor} = 0.92$, suggests that the dominant instabilities in the local simulation could potentially be affected by the global properties across the whole pedestal top and upper pedestal region—e.g. the structures are broad enough that they would extend to the regions ($\rho_{\rm tor} >$ 0.93) of much smaller local heat flux. To further investigate the radial structure of turbulence centered at $\rho_{\rm tor} = 0.92$, we examine the cross-correlations $C(\Delta x, 0)$ of $\Phi - \Phi$ and $\Phi - n$ as shown in figure 9. The half-width of $C(\Delta x, 0)$ is about $1.5\rho_s$ or $0.0075\rho_{\rm tor}$. It first reaches 0 when Δx becomes $4\rho_s$ or $0.02\rho_{\rm tor}$, suggesting that the most relevant range for the turbulence would be $\sim$0.90–$\sim$0.94.

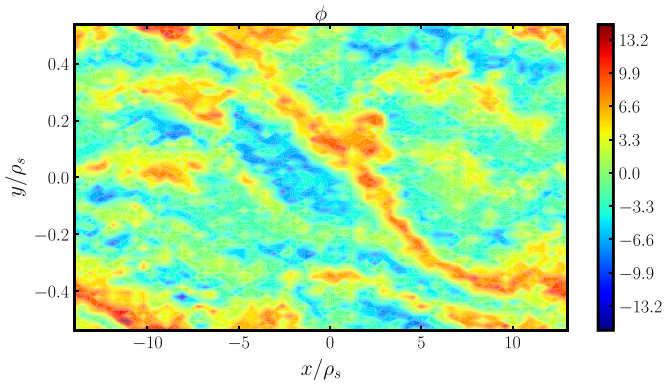

Figure 8. A time slice of the electrostatic potential at the intersection between the flux tube and the outboard mid-plane for the nonlinear local simulation at $\rho_{\rm tor} = 0.92$. The radially extended structure suggests that the dominant instabilities at $\rho_{\rm tor} = 0.92$ could be affected by the radial structure and properties in nonlinear global simulations.

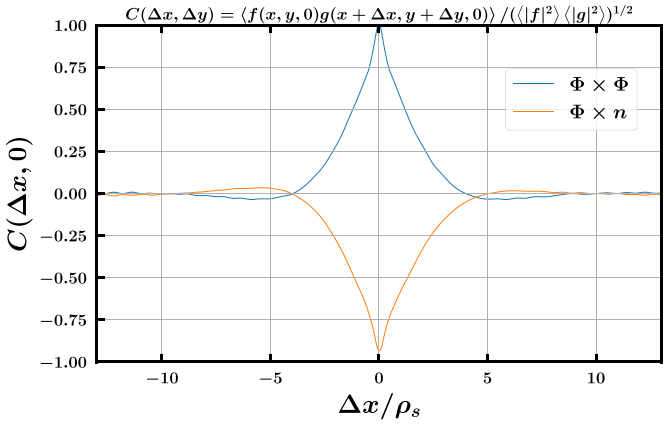

Figure 9. The cross-correlations $C(\Delta x, 0)$ of $\Phi - \Phi$ and $\Phi - n$ derived from the nonlinear local simulation at $\rho_{\rm tor} = 0.92$. The half-width for both is around $1.5\rho_s$ or $0.0075\rho_{\rm tor}$. $C(\Delta x, 0)$ drops to 0.25 when Δx reaches $2\rho_s$ or $0.01\rho_{\rm tor}$. The size of the relevant region is large enough to include strongly varying η regions in global simulations.

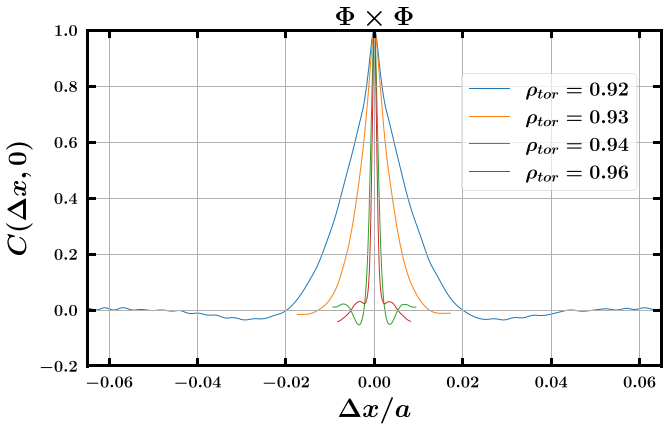

Figure 10. The cross-correlations $C(\Delta x, 0)$ of $\Phi - \Phi$ derived from the nonlinear local simulations for $\rho_{\rm tor} = 0.92$, 0.93, 0.94, and 0.96. The half-widths of $C(\Delta x, 0)$ are several times smaller for $\rho_{\rm tor} = 0.94$ and 0.96 compared to 0.92 and 0.93.

Figures 10 and 11 show the cross-correlations at several radial positions. At $\rho_{\rm tor} = 0.94$ and 0.96 the correlation lengths are much smaller compared to those at 0.92 and 0.93, which is consistent with the result that the local approximation is more accurate compared to the global result at these two locations.

The reason for the drastic change in radial correlation length can again be ascribed to the transition from toroidal ETG at the pedestal top (where the gradients are not too large–i.e. where the diamagnetic frequency ω_* and the magnetic drift frequency $\omega_{\rm D}$ are similar enough to stimulate a resonance) to slab ETG in the steep gradient region (where the gradients

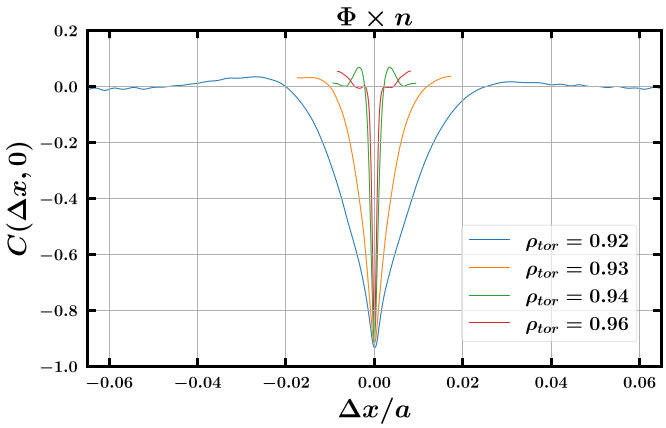

Figure 11. The cross-correlations $C(\Delta x, 0)$ of $\Phi - n$ derived from the nonlinear local simulations for $\rho_{\rm tor} = 0.92$, 0.94, and 0.96. Similar to the $\Phi - \Phi$ case, the half-widths of $C(\Delta x, 0)$ are several times smaller for $\rho_{\rm tor} = 0.94$ and 0.96 compared to 0.92 and 0.93.

are so steep that $\omega_* \gg \omega_{\rm D}$ and only slab resonances remain). Toroidal ETG is unstable only in regions of bad curvature at very small ballooning angle (corresponding to k_x), and consequently small radial structures are not excited to a high level and only the large radial structures persist. In contrast, pure slab ETG is insensitive to ballooning angle and so the small radial scales persist at substantial fluctuation amplitudes in the nonlinear state resulting in small radial correlation lengths.

Considering the impact of these observations on the turbulent properties, we refer to figure 1 and table 1. The results show that the temperature and density (and η) decrease significantly as $\rho_{\rm tor}$ is pushed outward within the range of 0.90–0.94. This decrease will inevitably weaken the ETG turbulence. On the other hand, other parameters such as the safety factor q and magnetic shear $\hat{s}$ vary weakly within this range and are therefore unlikely to explain the discrepancy between the global and local simulations at $\rho_{\rm tor} = 0.92$.

2.2. The effect of $E \times B$ shear

Another possible relevant mechanism is $E \times B$ shear suppression. Often flow shear is assumed to have little effect on ETG turbulence due to its small scales in time and space. However, the large radial structures observed in the pedestal top simulations may make them more susceptible to shear suppression. We note that all simulations described above include $E \times B$ shear. However, there is substantial uncertainty in the shear rate and so we conduct scans to probe sensitivities. The $E \times B$ shearing rate $\gamma_{E\times B}$ exhibits significant variability across the pedestal region, as illustrated in figure 12. $\gamma_{E\times B}$ has been calculated from the formula

$$\gamma_{E\times B} = \frac{\rho_{\rm tor}}{q}\frac{d}{d\rho_{\rm tor}}\frac{E_r}{B_\theta R} \tag{1}$$

where $\rho_{\rm tor}$ is the square root of the normalized toroidal flux, B_θ is the poloidal magnetic field, R is the major radius, q is the safety factor, $E_{\rm r}$ is the radial electric field estimated by the standard neoclassical formula [31],

$$V_{\parallel} = -\frac{RB_\phi}{ZeB}\left(\frac{1}{n_i}\frac{{\rm d}P_i}{{\rm d}\psi} + Ze\frac{{\rm d}\Phi_0}{{\rm d}\psi} - k_{\parallel}\frac{B^2}{\langle B\rangle^2}\frac{{\rm d}T_i}{{\rm d}\psi}\right) \tag{2}$$

by setting the parallel flow $V_{\parallel}$ to zero, which follows the same procedure as adopted in [12, 17], where B_ϕ is the toroidal magnetic field, P_i is ion pressure, Φ_0 is the electrostatic potential, and ψ is the normalized poloidal magnetic flux,

At $\rho_{\rm tor} = 0.92$, the shearing rate is only 0.058, but increases to -0.126 at $\rho_{\rm tor} = 0.93$ and -0.311 at $\rho_{\rm tor} = 0.94$. While these values may appear small for electron-scale turbulence, they are more comparable to the growth rates of ion-scale turbulence, which has the potential to reduce heat flux. To investigate this, nonlinear local simulations were conducted for $\rho_{\rm tor} = 0.92$, and figure 13 shows the corresponding $\gamma_{E\times B}$ scans. The results reveal that the heat flux decreases significantly as $\gamma_{E\times B}$ increases, with an 85% reduction observed when $\gamma_{E\times B}$ increases by a factor of 10. As $\gamma_{E\times B}$ is increased further, the heat flux can be suppressed even more, potentially reaching a value of 0.54 MW when $\gamma_{E\times B}$ is equal to 2.5. It is worth noting that these values for $\gamma_{E\times B}$ were chosen as approximations of the shearing rate at $\rho_{\rm tor} = 0.94$ (which is one radial correlation length from $\rho_{\rm tor} = 0.92$) and 0.96 (close to the simulated boundary of $\rho_{\rm tor} = 0.92$), in order to investigate the possible maximum effect of shearing on turbulence.

2.3. Parameterizing the breakdown of the local flux tube approximation

The above analysis shows the ETG turbulence in the pedestal top for MAST can be affected by the global properties, which is also shown for some systems with ETG turbulence [28]. The background magnetic fields of spherical tokamaks are mostly less than 1 T with ~0.5 T in our case for MAST, which is much weaker than most cases for conventional tokamaks. The weaker magnetic field results in larger normalize gyroradius $\rho_* = \rho_s/a$ and therefore leads to comparatively larger fluctuation scales. Combined with the fact that the pedestal is intrinsically narrow, the size of the pedestal top transition region then becomes only $\sim 5\rho_s$. If the ensuing turbulence has radially extended structures, the local approximation breaks down

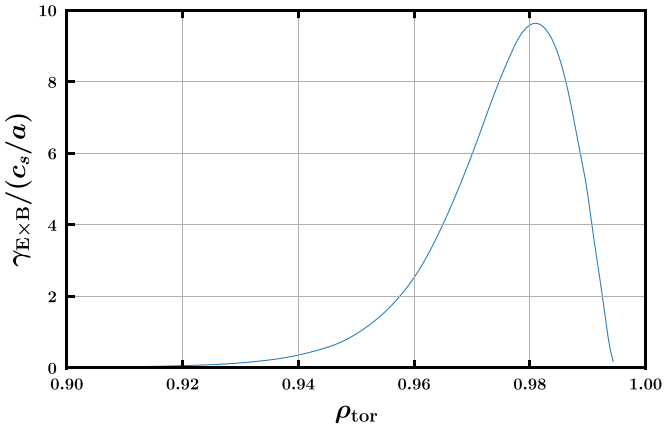

Figure 12. The $E \times B$ shearing rate $\gamma_{E\times B}$ is nearly zero in the pedestal top and becomes significantly larger at the upper and mid pedestal region. Instabilities with extended structure in radial direction emerged in local simulations in the pedestal top can be affected by the shear.

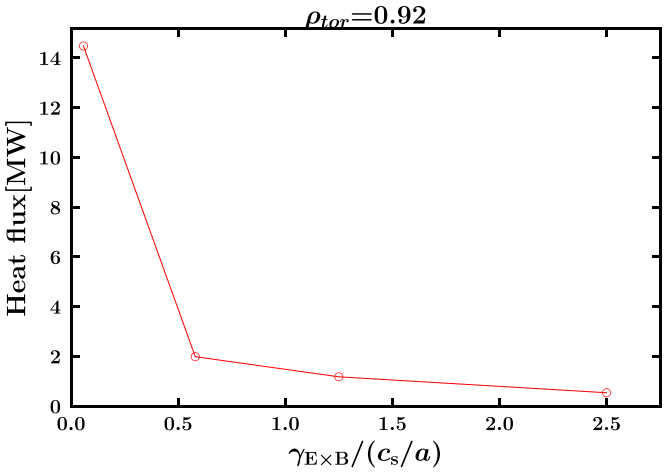

Figure 13. Heat flux versus the $E \times B$ shearing rate $\gamma_{E\times B}$. Heat flux decreases significantly as $\gamma_{E\times B}$ increases, with a 85% decrease when $\gamma_{E\times B}$ becomes 10 times larger. The heat flux can eventually reach a physical value of 0.54 MW when $\gamma_{E\times B}$ is equal to 2.5.

because profiles, gradients and $\gamma_{\mathrm{E\times B}}$ vary over the required simulation domain, and global calculations are required that take this into account.

The aforementioned analysis provides a qualitative explanation, but it is imperative to conduct quantitative assessments to ascertain the validity of the local approximation. The local flux tube approximation firstly assumes the density gradient scale length, denoted as $L_n = -\frac{n}{\mathrm{d}n/\mathrm{d}x}$, and the temperature gradient length scale, denoted as $L_T = -\frac{T}{\mathrm{d}T/\mathrm{d}x}$, can be approximated as constants across the simulated region, and then secondly employs periodic boundary conditions. We define the correlation length in the radial direction, Δ_x, as the width of $C(\Delta x, 0)$ of ϕ that first crosses zero, as illustrated in figure 10. To evaluate its significance in relation to other length scales, the density profile is initially investigated to verify the fulfillment of various relevant conditions.

Expanding $\frac{\nabla n}{n}(x)$ to the first order, $\frac{\nabla n_0}{n_0} + x\frac{n_0\nabla^2 n_0 - (\nabla n_0)^2}{n_0^2}$, it becomes apparent that the correlation length in the radial direction, Δ_x, must satisfy the first condition $\Delta_x \ll |\frac{\nabla n_0}{n_0}| \,/\, |\frac{n_0\nabla^2 n_0 - (\nabla n_0)^2}{n_0^2}|$ when approximating $\frac{\nabla n}{n}(x)$ with $\frac{\nabla n_0}{n_0}$. In addition, Δ_x should also be smaller than L_n and L_T to ensure the validity of the periodic boundary condition, specifically $|\Delta_x/L_n|$ and $|\Delta_x/L_T| \ll 1$ as the second condition. The local approximation breaks down if any of the aforementioned conditions is violated. The outcome of the first condition is depicted in figure 14, where it is evident that the condition is violated at $\rho_{\mathrm{tor}} = 0.92$ and 0.93, while being satisfied at $\rho_{\mathrm{tor}} = 0.94$ and 0.96. Although this does not provide insights into how turbulence is affected by higher-order terms, it directly indicates the breakdown of the local approximation at these radial locations due to profile curvature. The second condition and a similar analysis for T exhibit satisfactory fulfillment at these radial positions but is not presented here.

We note that this analysis points to the significant role played by the curvature of the density profile, denoted as $\nabla^2 n$, in determining the validity of the local approximation in this MAST equilibrium. In the absence of the curvature term, the first and second conditions are mathematically equivalent, denoted as $|\Delta_x/L_n| \ll 1$, and their fulfillment is observed across all cases examined in this study. This finding suggests that the curvature of the profiles can significantly influence the turbulent transport, in particular by stabilizing the ETG modes in this case. An interesting analysis would be to explore

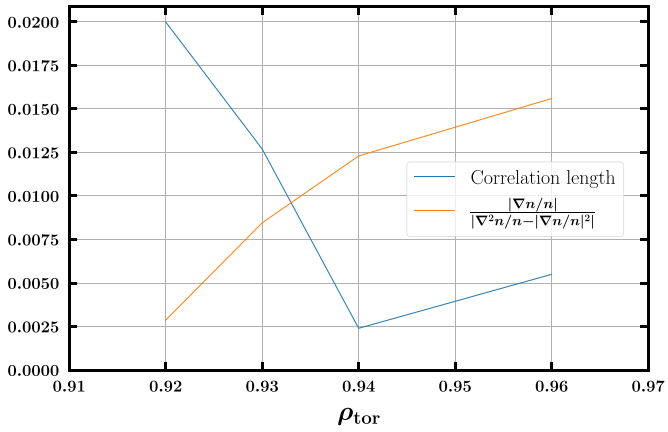

Figure 14. The condition $\Delta_x \ll |\frac{\nabla n_0}{n_0}|/|\frac{n_0\nabla^2 n_0-(\nabla n_0)^2}{n_0^2}|$ is violated at $\rho_{\rm tor}=0.92$ and 0.93 while being satisfied at $\rho_{\rm tor}=0.94$ and 0.96. The local approximation is therefore invalid at $\rho_{\rm tor}=0.92$ and 0.93.

the effects brought by the profile curvature (the second-order derivative of the profile) described [32, 33]. However, the precise manner in which the curvature of the profiles impacts different micro-instabilities remains an unresolved question, warranting future investigation. Based on the analysis conducted in this section, it is concluded that nonlocal effects are critical in the transition from the steep gradient region to the pedestal top.

3. Local post-ELM simulations

While the pre-ELM stage may be the most important due to its direct reflection of the pedestal structure (and its connection to confinement), we are also interested in the post-ELM stage, which reflects the early recovery process of the pedestal. Again as figures 15 and 16 show, three radial locations $\rho_{\rm tor}=0.966, 0.976, 0.986$ that cover the upper pedestal to mid pedestal region are selected to study the ETG turbulence during post-ELM stage. Table 3 shows the physical input parameters for the simulations. All parameters except $\omega_{\rm n}$ and $\omega_{\rm T}$ are smaller than the pre-ELM analysis presented previously.

Figure 17 shows the growth rate spectrum at three different radial locations. The peak of the growth rate spectrum moves toward smaller scales as $\rho_{\rm tor}$ increases while the growth rate spectrum is similar at large scales $k_y<100$. By utilizing simple mixing length estimates on the growth rate spectrum with similar k_x, we can naively expect ETG turbulence to be stronger at $\rho_{\rm tor}=0.976$ than 0.986 since the growth rates for the former at large scales are a bit larger along with the fact that $T_{\rm ref}$ is also larger at this radial location. As for $\rho_{\rm tor}=0.966$, it is not enough to predict whether ETG turbulence is more prominent here compare to 0.976 and 0.986 just by using simple mixing length estimates because the spectrum remains to be slightly below those from the two at large scales while $T_{\rm ref}$ is larger.

Figure 18 shows the heat fluxes calculated at these radial locations. It is not surprising, that the electron heat flux is small at $\rho_{\rm tor}=0.986$ due to the low temperature and η. On the other hand, the ETG turbulence at $\rho_{\rm tor}=0.976$ is produces 0.31 MW of heat flux which is similar to the pre-ELM case at the pedestal top region $\rho_{\rm tor}=0.94$, suggesting the ETG turbulence is pushed toward the core during the inter-ELM period. By comparing the profiles from figures 1 and 15, one can see that the temperature profiles are basically the same with the turning point or, the part with larger temperature profile curvature, straightened and moved from $\sim$0.965 to $\sim$0.94. On the contrary, the density profile keeps building up with the density on the pedestal top increases from $\sim 2.75\times10^{19}\,{\rm m}^{-3}$ to $\sim 3.9\times10^{19}\,{\rm m}^{-3}$during the period, while the turning point is pushed from $\sim$0.97 to 0.94. This indicates that peak η around the pedestal top is pushed inward during the inter-ELM period. While it is known that the heat flux produced by ETG turbulence depends on η and $T_{\rm ref}$, it should also be pushed inward with its magnitude increased as peak η moves inward, which agrees with the result presented here. Note that same behavior is observed for MTMs in MAST pedestal presented in [22].

Figure 19 shows the sensitivity of linear growth rates to equilibrium gradients in the post-ELM equilibrium at $\rho_{\rm tor}=0.976$. Growth rates at the larger scale doubled when there are 20% increase in $a/L_{\rm T0}$ and 20% decrease in $a/L_{\rm n0}$, implying that the heat flux produced by the ETG turbulence at this stage can reach a higher saturation level within the measurement error.

The heat fluxes obtained from nonlinear local gyrokinetics simulations considering the post-ELM stage at $\rho_{\rm tor}=0.976$ is shown in figure 20. The simulations also show that the heat flux increases significantly when there is a 20% increase in $a/L_{\rm T0}$ and a 20% decrease in $a/L_{\rm n0}$. To be more precise, the post-ELM case shows a $\sim$300% increase in heat flux, which is more dramatic than at $\rho_{\rm tor}=0.94$ during the pre-ELM stage. Again, this value is much higher than expected from linear simulations, which shows a growth rate increase of only $\sim$100%.

With regard to the fact that ETG is also shown to be active during pre-ELM stage around the upper pedestal to the pedestal top region, ETG can be regarded as excited during the inter-ELM period. Also, since both figures 6 and 20 show substantial heat flux increase when η is adjusted within

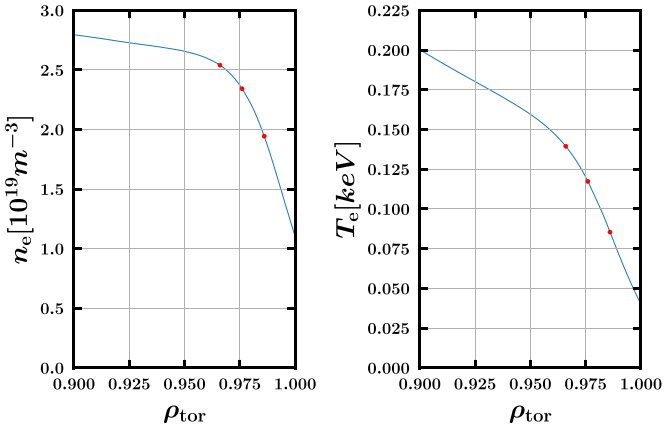

Figure 15. The electron density and temperature versus the normalized toroidal flux surface label ρ_{tor} during post-ELM stage.

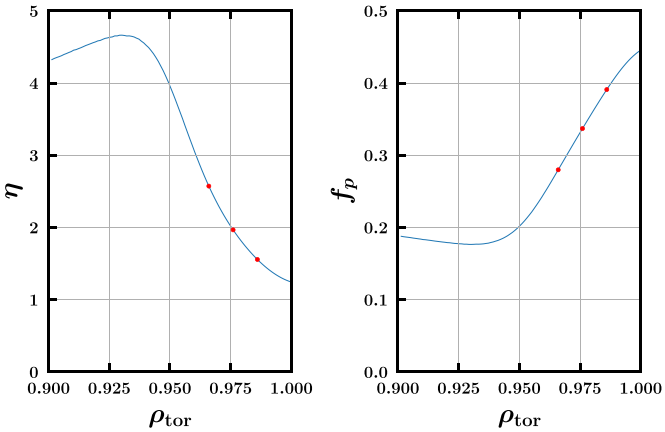

Figure 16. η and f_p versus the normalized toroidal flux surface label ρ_{tor} during post-ELM stage.

Table 3. The common physical input parameters at $\rho_{tor} = 0.966, 0.976, 0.986$, respectively. η and β decrease as ρ_{tor} increases. Magnetic shear does not vary a lot around the pedestal top.

ρ_{tor}	q_0	$\hat{s}$	ω_n	ω_T	η	β	B_{ref}	T_{ref}	n_{ref}
0.966	6.72	4.71	4.98	12.5	2.51	0.0058	0.495	0.140	2.54
0.976	7.05	4.67	12.2	23.4	1.92	0.0045	0.495	0.117	2.34
0.986	7.41	4.98	27.0	41.2	1.53	0.0027	0.495	0.085	1.94

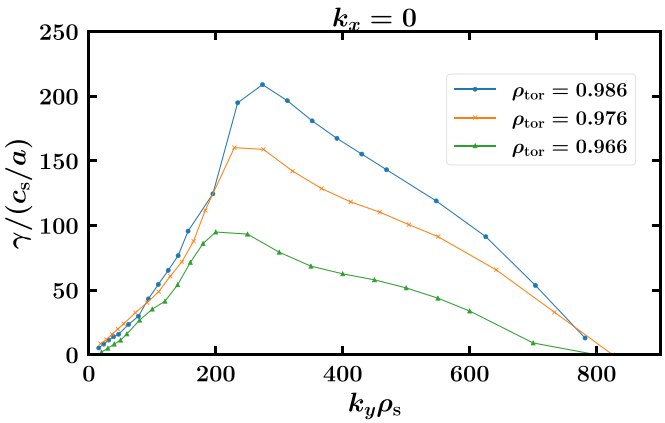

Figure 17. The growth rate spectrum for three radial locations $\rho_{tor} = 0.966, 0.976, 0.986$ during the post-ELM stage with c_s and ρ_s calculated at $\rho_{tor} = 0.966$.

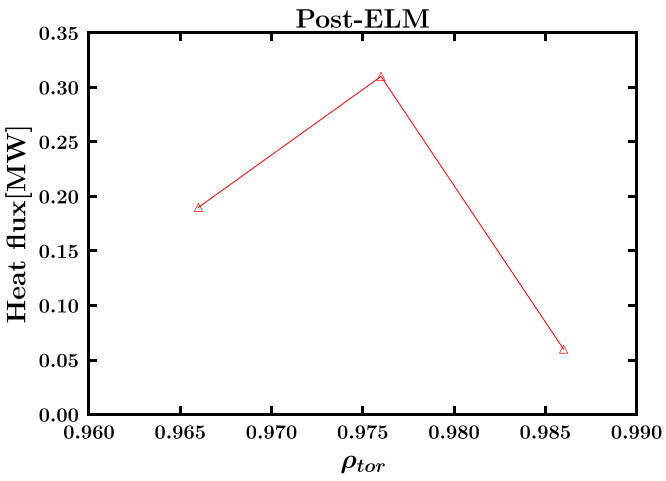

Figure 18. The growth rate spectrum for three radial locations $\rho_{\rm tor} = 0.966, 0.976, 0.986$ during the post-ELM stage.

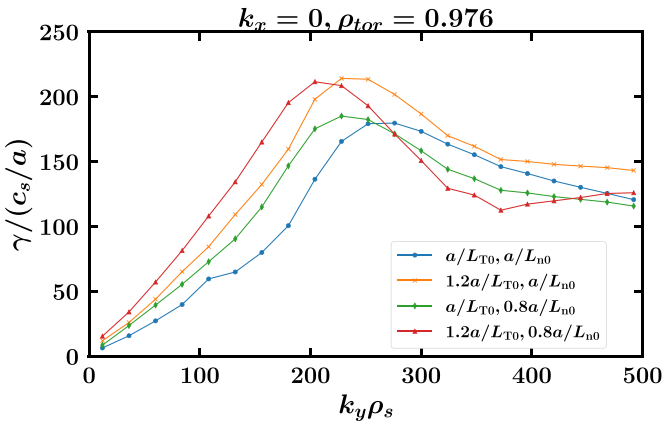

Figure 19. Growth rate spectrum at $\rho_{\rm tor} = 0.976$ during the post-ELM stage. The spectrum is moved upward about 60% when the temperature gradient $a/L_{\rm T0}$ is increased by 20%, and moved horizontally toward the larger scale when $a/L_{\rm n0}$ is decreased.

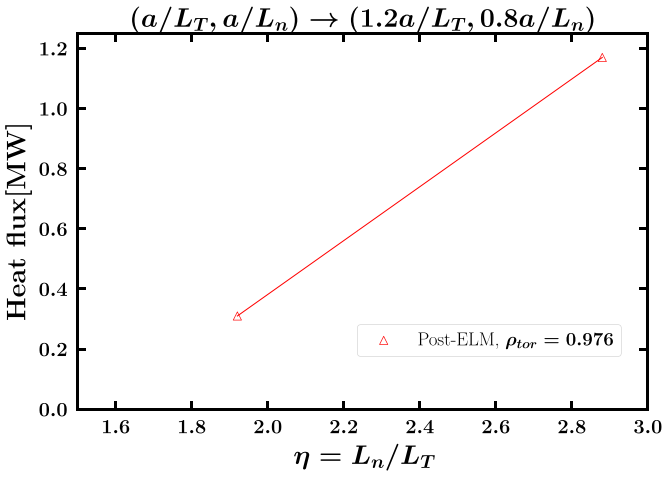

Figure 20. Heat fluxes calculated at $\rho_{\rm tor} = 0.976$ for the post-ELM stage shows the heat flux increased significantly when there is a 20% increase in $1/L_{\rm T0}$ and a 20% decrease in $1/L_{\rm n0}$. The amount of heat flux increased is more profound than the pre-ELM stage.

the error bar, ETG turbulence is very likely to be playing an important role in pedestal formation, probably the temperature pedestal height, by relaxing the temperature profile around the upper pedestal to the pedestal top region in MAST. Note that ETG in this MAST discharge does not appear to be responsible for limiting gradients since it is absent in the steep pedestal region, unlike in some machines like JET [16, 17, 20].

4. Conclusion

This paper presents local and global gyrokinetic analysis of ETG turbulence and transport in the MAST pedestal. Our results suggest that ETG turbulence likely plays a significant role in transport in spherical tokamaks in the upper pedestal and pedestal top regions. This is true both in a pre-ELM phase immediately prior to an ELM as well as a post-ELM phase when the pedestal is recovering and the temperature profile is rebuilding. Simulations produce transport levels on the order of 1 MW (compared to 4 MW total heating power), showing that ETG turbulence may have been constraining the temperature pedestal top along with MTM. The heat flux also strongly increases with the temperature gradient, indicating stiff transport.

One major result of this paper is that the flux tube approximation breaks down at the pedestal top, where we observe that local simulations produce unrealistically high transport levels while global simulations produce much lower transport levels. We attribute the breakdown of the local approximation to large radial structures that emerge in the local nonlinear simulations. Large-scale structures sample the entire structure of the equilibrium profile not just its local gradients. The breakdown of the flux tube approximation can be parameterized by the ratio of the radial correlation length to a length scale representative of profile curvature; the local and global simulations agree when this ratio is sufficiently smaller than unity. The difference between the local and global stability of an eigenvalue problem is a well-known phenomenon. An extreme case is when the system is locally unstable everywhere but is globally stable [34]. Whether the stabilization of ETG observed at $\rho_{\rm tor} = 0.92$ from global effect is linear (smaller growth rate) or nonlinear (stronger nonlinear energy transfer) will be left for future research.

Overall, this study provides insight into the mechanisms behind the formation of the MAST pedestal and may inform strategies such as injecting beams to modify the profiles in the targeted region to produce localized global effects (ETGs can experience global effects if the radial scale is not small, shown in section 2) or increase density gradient (ETGs in the pedestal are stiff, shown in section 2) for optimizing the edge plasma of spherical tokamaks, thus enhancing confinement. Note that the study of the saturation mechanisms of the ETG turbulence in MAST which we conclude the forward cascade is the major contributor is described in appendix A for further reading.

Acknowledgments

This work is supported by U.S. Department of Energy under Grant Nos. DE-SC0019102, DE-FG02-04ER54742, and the EPSRC Energy Programme under Grant No. EP/W006839/1.

Appendix A. ETG saturation mechanism

In addition to determining the presence of ETG turbulence in the pedestal, it is important to investigate the mechanisms by which ETG turbulence reaches saturation within the pedestal. One can begin with the gyrokinetic equation for the perturbed distribution function $g_{j,k}$ (sometimes called the generalized distribution function) for species j (see [35] for details and normalizations). Its evolution is governed by the gyrokinetic Vlasov equation $\partial g_{j,k}/\partial t = L[g_{j,k}] + N[g_{j,k}]$, where L and N represent the linear and nonlinear operators, with

$$\begin{aligned} L[g_{j,k}] = &-\omega_* F_{j0} i k_y \chi_{j,k} + \frac{\beta T_{j0}}{q_j B_0^2} v_\parallel^2 \omega_p \Gamma_{y,j,k} - \frac{v_{{\rm T}j}}{JB_0} v_\parallel \Gamma_{z,j,k} \\ &- \frac{T_{j0}\left(2v_\parallel^2 + \mu B_0\right)}{q_j B_0}\left(K_y \Gamma_{y,j,k} + K_x \Gamma_{x,j,k}\right) \\ &+ \frac{v_{{\rm T}j}}{2JB_0} \mu \partial_z B_0 \frac{\partial f_{j,k}}{\partial v_\parallel} + \langle C_{j,k}(f) \rangle , \end{aligned} \tag{3}$$

and

$$N[g_{j,k}] = \sum_{k'} \left(k_x' k_y - k_x k_y'\right) \chi_{j,k'} g_{j,k''} , \tag{4}$$

where $\mathbf{k}'' = \mathbf{k} - \mathbf{k}' = (k_x - k_x', k_y - k_y')$, $\omega_* = \omega_{{\rm n},j,k} + (v_\parallel^2 + \mu B_0 - 3/2)\omega_{{\rm T},j,k}$, while $f_{j,k} = g_{j,k} - \frac{2q_j}{m_j v_{{\rm T}j}} \bar{A}_{\parallel,k} F_{j0}$ is the total perturbed distribution function, $\chi_{j,k} = \bar{\Phi}_k - v_{Tj} v_\parallel \bar{A}_{\parallel,k}$ is the modified potential, v_{Tj} is the species-dependent thermal velocity, $\bar{\Phi}_k$ is the gyroaveraged electric potential, $\bar{A}_{\parallel,k}$ is the gyroaveraged parallel magnetic potential, $v_\parallel$ is the parallel velocity, n_{j0} is the background density, T_{j0} is the background temperature, q_j is the charge, F_{j0} is the background Maxwellian, $\mathbf{v} = (v_\parallel, \mu)$ is the velocity vector, $\omega_p = a/L_p$ is the normalized pressure gradient, $K_{x,y}$ are the curvature terms, $\Gamma_{x,y} = i k_{x,y} g + \frac{q_j}{T_{j0}} F_{j0} i k_{x,y} \chi$, and $\Gamma_z = \partial_z g + \frac{q_j}{T_{j0}} F_{j0} \partial_z \chi + \frac{v_{{\rm T}j} q_j}{T_{j0}} v_\parallel \mu F_{j0} \bar{A}_{\parallel,k} \partial_z B_0$.

Note that $L[g_{j,k}]$ consists of the terms of gradient drive, pressure, parallel dynamics, curvature, trapping, and collisions in order. With the above definitions, one can define the energy exchange rate through nonlinearities $\mathrm{d}E/\mathrm{d}t|_{\rm nl}$, the energy injection rate from the drive $\mathrm{d}E/\mathrm{d}t|_{\rm drive}$, and collisional energy dissipation rate $\mathrm{d}E/\mathrm{d}t|_{\rm col}$, and the numerical energy dissipation rate $\mathrm{d}E/\mathrm{d}t|_{\rm diss}$ in the total time derivative of the energy $\mathrm{d}E_{{\rm tot},k}/\mathrm{d}t$ at wavenumber k as

$$\begin{aligned} \left.\frac{\mathrm{d}E_k}{\mathrm{d}t}\right|_{\rm nl} = 2{\rm Re}\Bigg\{ &\sum_{k',j} \int \frac{n_{j0} T_{j0}}{F_{j0}} \left[g_{j,k} + \frac{q_j F_{j0}}{T_{j0}} \chi_{j,k} \right]^* \\ &\times \left(k_x' k_y - k_x k_y'\right) \chi_{j,k'} g_{j,k''} \mathrm{d}z \mathrm{d}v \Bigg\} \end{aligned}$$

$$\left.\frac{\mathrm{d}E_k}{\mathrm{d}t}\right|_{\rm drive} = -2{\rm Re}\left\{ \sum_j \int \pi n_{j0} T_{j0} i k_y \nu_* g_{j,k}^* \chi_{j,k} \mathrm{d}z \mathrm{d}v \right\}$$

$$\left.\frac{\mathrm{d}E_k}{\mathrm{d}t}\right|_{\{\rm diss,col\}} = -2{\rm Re}\left\{ \sum_j \int \pi n_{j0} T_{j0} \Gamma_{j,k}^* C_{\{\rm diss,col\}j,k}(f) \mathrm{d}z \mathrm{d}v \right\}, \tag{5}$$

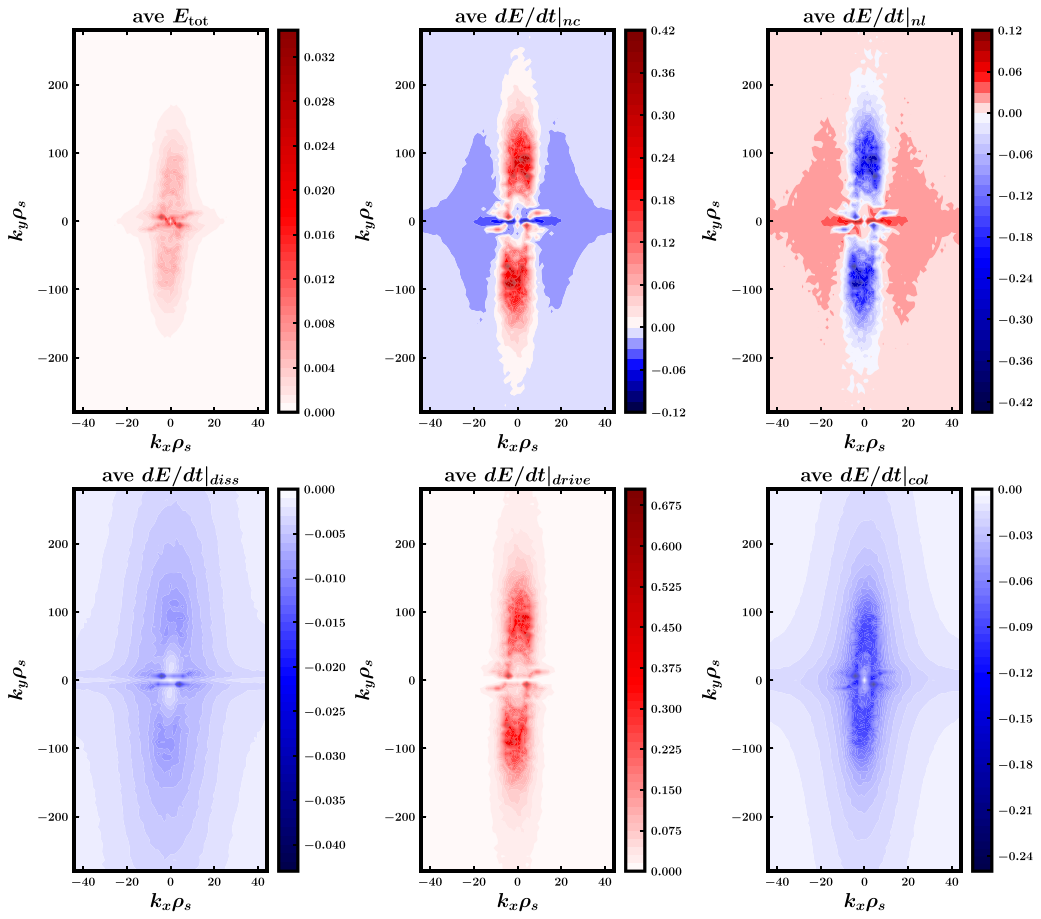

Figure 21. The energy and $\mathrm{d}E/\mathrm{d}t$ contour plots at $\rho_{\rm tor} = 0.94$ during the pre-ELM stage. The $E|_{\rm tot}$ contour plot shows the streamers are excited, with $\mathrm{d}E/\mathrm{d}t|_{\rm drive}$ contour plot showing them injecting energy into the system. The energy is distributed across all scales via nonlinear processes and removed by collisions at all scales according to the $\mathrm{d}E/\mathrm{d}t|_{\rm nl}$ and $\mathrm{d}E/\mathrm{d}t|_{\rm col}$ contour plots. $\mathrm{d}E/\mathrm{d}t|_{\rm nc}$ contour plot shows forward and backward energy cascades are present.

where $\Gamma_{j,k} = f_{j,k} + \frac{q_j F_{j0}}{T_{j0}}\bar{\phi}$, and the non-conservative rate of change of energy $\mathrm{d}E/\mathrm{d}t|_{\rm nc}$ is the sum of $\mathrm{d}E/\mathrm{d}t|_{\rm diss}$, $\mathrm{d}E/\mathrm{d}t|_{\rm drive}$, and $\mathrm{d}E/\mathrm{d}t|_{\rm col}$ [36, 37]. In this section of the appendix, we focus on the saturated state at $\rho_{\rm tor} = 0.94$ for the pre-ELM stage and $\rho_{\rm tor} = 0.976$ for the post-ELM stage by doing similar triplet diagnostics and energy transfer analysis presented in [37].

The contour plots depicted in figure 21 offer valuable insights into the time-averaged energy flow in k-space during the saturation of ETG turbulence at $\rho_{\rm tor} = 0.94$ in the pre-ELM stage. The contour plot for $E|_{\rm tot}$ reveals strong excitation of low k_x modes with $k_y \lesssim 180$, which aligns with the expected behavior since energy injection predominantly occurs within this range, as indicated by the $\mathrm{d}E/\mathrm{d}t|_{\rm drive}$ contour plot. Subsequently, nonlinear processes redistribute the energy across all scales, as observed in the $\mathrm{d}E/\mathrm{d}t|_{\rm nl}$ contour plot.

One can also observe that a tilted $E|_{\rm tot}$ contour plot in our simulation results. Analysis revealed that this phenomenon is a result of the $E \times B$ shear. However, it is expected that the magnitude of this effect was not sufficient to suppress the ETG turbulence, as the growth rates of the low k_x modes are significantly larger ($\gtrsim 1$) than the $E \times B$ shearing rate $\gamma_{E\times B} = -0.311$.

The primary mechanism for the dissipation of the energy is through collisions which dominate over numerical dissipation. Analysis of the $\mathrm{d}E/\mathrm{d}t|_{\rm nc}$ contour plot reveals substantial energy removal at all range. From figure 3, one can find that the growth rate in the large-scale range ($k_y < 20$) is non-zero, suggesting that large-scale stable modes are also excited which leads to net energy removal in this range. Additionally, zonal modes are observed removing energy actively, though not the dominant energy sink for the saturation balance, through damping.

While it is commonly assumed that the primary mechanism for energy dissipation is through the forward cascade, the data presented in figure 21 suggests that inverse cascade and zonal mode damping also contribute to some level of energy removal. Note that the inverse energy cascade for ETG turbulence is also observed in various cases[28, 37].

While zonal modes are actively dissipating energy, does zonal-flow catalyzed nonlinear energy transfer plays an important role in saturating ETG turbulence? From the total energy contour plot in figure 21, one can see that zonal modes are excited but not prominent relative to the low k_x modes, therefore, zonal flow-catalyzed energy transfer might not be conspicuous. Figure 22 shows the nonlinear transfer rate $T_{{\rm nl},k}$

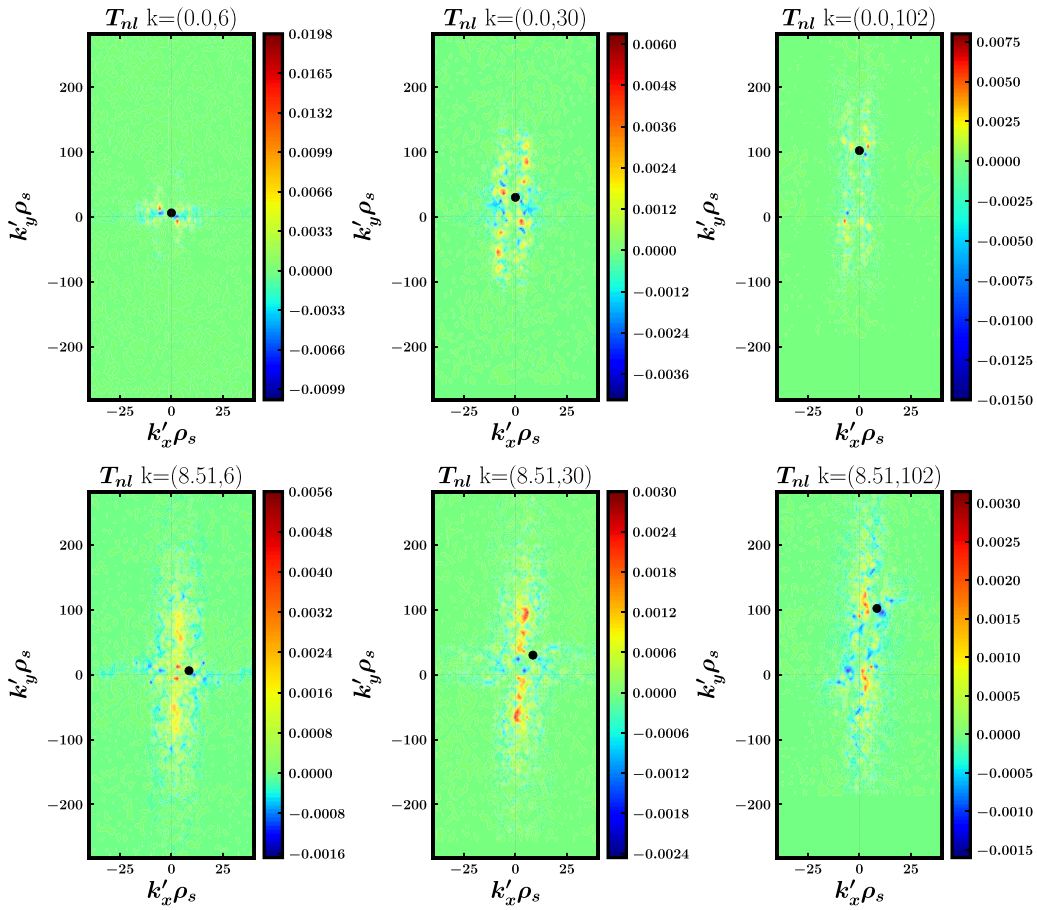

Figure 22. Triplet diagnostics $T_{\mathrm{nl},k}$ for various wavenumbers at $\rho_{\mathrm{tor}} = 0.94$ during pre-ELM stage. The $k = (0, 0.6)$ contour plot shows backward energy cascade is driven by large-scale $k_x \neq 0$ modes. Other contour plots show typical forward energy cascade is present.

contour plots for six different wavenumbers where $T_{\mathrm{nl},k}$ is defined as

$$T_{\mathrm{nl},k} = 2\mathrm{Re}\left\{\sum_j \int \frac{n_{j0}T_{j0}}{F_{j0}}\left[g_{j,k} + \frac{q_j F_{j0}}{T_{j0}}\chi_{j,k}\right]^* \times \left(k'_x k_y - k_x k'_y\right)\chi_{j,k'}\, g_{j,k''}\, \mathrm{d}z\mathrm{d}v\right\}. \quad (6)$$

Note that in the contour plots, the color red indicates that the modes at wavenumber k are driving energy through the triplet interaction involving k', while the color blue implies the opposite behavior. For the large-scale streamer at $k = (0, 6)$, it mostly interacts with modes with similar k_y at low k_x; energy is transferred to it from the highly excited unstable modes around $k = (4.3, -12)$ and $k = (-4.3, 12)$. However, no sign shows the modes at $k = (0, 6)$ strongly interact with zonal modes. The backward cascade observed from the $\mathrm{d}E/\mathrm{d}t|_{\mathrm{nc}}$ contour plot in figure 21 is therefore majorly driven by the large scale unstable modes with non-zero k_x.

For small-scale streamers at $k = (0, 30)$ and $(0, 102)$, the magnitude of the outgoing energy transfer represented by blue regions in the contour plot of $T_{\mathrm{nl},k}$ is broadly distributed at lower $k'_y < k_y$ denoting an inverse cascade. In terms of the radial scales it peaks at $k'_x \sim \pm 4.2$ with k'_y.

The $T_{\mathrm{nl},k}$ contour plots for $k = (8.51, 6)$, $(8.51, 30)$, and $(8.51, 102)$ show the red regions are at lower k'_x while the blue regions are at higher k'_x, implying that the sidebands are strongly interacting with lower k_x modes by carrying away energy. This is a clear sign of a forward energy cascade in the radial direction. Again, the sidebands do not strongly interact with the zonal modes, both the forward and backward energy cascade observed in $\mathrm{d}E/\mathrm{d}t|_{\mathrm{nc}}$ contour plot in figure 21 are mostly driven by non-zonal catalyzed interactions. The ETG turbulence at $\rho_{\mathrm{tor}} = 0.94$ is therefore still mostly saturated by forward cascade in the radial direction with to small-scale stable regions as energy sinks, while there is inverse transfer to large-scale stable modes and zonal modes in the binormal direction.

Appendix B. Simulation setup

Table 4 presents the resolutions utilized in various nonlinear simulations. The table includes the following parameters: ρ_{tor}, which represents the radial location; n, denoting the number of gridpoints in each dimension; and L, indicating the box size. The subscripts used for n and L are as follows: s for species,

Table 4. Resolutions used for different nonlinear runs. $k_{y,\min}$ is set to 6 for pre-ELM simulation at $\rho_{\rm tor}$ to avoid MTMs that keep the turbulence away from saturation. n_w is set to 32, which is exceptionally high for post-ELM simulation at $\rho_{\rm tor} = 0.986$ to avoid positive energy injection from collision raised from numerical issue.

$\rho_{\rm tor}$	n_x	n_{k_y}	n_z	n_w	$k_{y,\min}\rho_s$	L_x
			Local Pre-ELM			
0.92	64	32	64	16	6	27.0
0.93	64	96	96	16	2	10.9
0.94	64	192	84	16	2	4.11
0.96	64	256	84	16	2	4.05
			Global Pre-ELM			
0.905–0.975	256	48	64	16	12.04	15
			Local Post-ELM			
0.966	128	48	256	16	12	3.98
0.976	128	64	280	24	12	4.39
0.986	128	48	512	32	12	4.4

x for the radial direction, y for the bi-normal direction, z for the parallel direction, v for the parallel velocity space, and w for the magnetic moment. Moreover, $k_{y,\min}\rho_s$ represents the minimum wavenumber in the bi-normal direction.

For all simulations, certain values remain the same and are not explicitly displayed in the table. These include $n_s = 2$, $n_v = 36$, $L_v = 3$, and $L_w = 9$. The Arakawa_zv is on to incorporate parallel and parallel velocity derivatives within a Poisson bracket structure and is solved using an Arakawa scheme to prevent nonlinear computational instability [38].

Note that simulations conducted at outer radial locations necessitate higher n_z values, especially during the post-ELM period. Additionally, for enhanced resolution at the outboard mid-plane, the parameter edge_opt is set to 8. It is important to mention that the calculated saturated heat fluxes for the pre-ELM cases, using $k_{y,\min} = 6$ and 12, exhibit an error within 10%. Simulations with $k_{y,\min} = 2$ are carried out to investigate the impact of close-ion-scale ETG modes. In most simulations, the saturated heat flux remains relatively unaffected, except for the case at $\rho_{\rm tor} = 0.92$, where MTMs become dominant and do not exhibit turbulence saturation. It is also important to note that the simulations were run on various machines, each with either 56 or 64 cores per node. Consequently, the choice of n_z values is based on selecting multiples of 7 or 8 to effectively utilize the computational power of these supercomputers. It should be noted that all global simulations were conducted employing the resolution outlined in table 4 with the exception of an additional global simulation run with higher resolution utilizing a larger box spanning the range $\rho_{\rm tor} = 0.88$–0.973 alongside a lower wavenumber $k_{y,\min} = 2$ for convergence check. It is also used to confirm that the boundary conditions has minor influence on the computed heat flux in the pedestal top.

In the post-ELM simulation at $\rho_{\rm tor} = 0.986$, a high n_w resolution is employed to mitigate positive energy input resulting from collisions caused by numerical errors.

ORCID iDs

P.-Y. Li https://orcid.org/0000-0002-9525-4171
D.R. Hatch https://orcid.org/0000-0002-1625-4385
B. Chapman-Oplopoiou https://orcid.org/0000-0001-9879-2285
C.M. Roach https://orcid.org/0000-0001-5856-0287

References

[1] Wagner F. *et al* 1982 *Phys. Rev. Lett.* **49** 1408
[2] Connor J.W. 1998 *Plasma Phys. Control. Fusion* **40** 531
[3] Jenko F. 2000 *Comput. Phys. Commun.* **125** 196
[4] Görler T., Lapillonne X., Brunner S., Dannert T., Jenko F., Merz F. and Told D. 2011 *J. Comput. Phys.* **230** 7053
[5] Dorland W., Jenko F., Kotschenreuther M. and Rogers B.N. 2000 *Phys. Rev. Lett.* **85** 5579
[6] Jenko F. and Dorland W. 2002 *Phys. Rev. Lett.* **89** 225001
[7] Guttenfelder W. *et al* 2022 *Nucl. Fusion* **62** 042023
[8] Jenko F., Told D., Xanthopoulos P., Merz F. and Horton L.D. 2009 *Phys. Plasmas* **16** 055901
[9] Hatch D.R., Told D., Jenko F., Doerk H., Dunne M.G., Wolfrum E., Viezzer E. and Pueschel M.J. 2015 *Nucl. Fusion* **55** 063028
[10] Hatch D.R., Kotschenreuther M., Mahajan S., Valanju P. and Liu X. 2017 *Nucl. Fusion* **57** 036020
[11] Kotschenreuther M., Hatch D.R., Mahajan S., Valanju P., Zheng L. and Liu X. 2017 *Nucl. Fusion* **57** 064001
[12] Hatch D.R. *et al* 2019 *Nucl. Fusion* **59** 086056
[13] Kotschenreuther M. *et al* 2019 *Nucl. Fusion* **59** 096001
[14] Liu X., Kotschenreuther M., Hatch D.R., Mahajan S.M., Hughes J.W. and Hubbard A.E. arXiv:2005.08924
[15] Hatch D.R. *et al* 2022 *Phys. Plasmas* **29** 062501
[16] Guttenfelder W., Groebner R., Canik J., Grierson B., Belli E. and Candy J. 2021 *Nucl. Fusion* **61** 056005
[17] Chapman-Oplopoiou B. *et al* 2022 *Nucl. Fusion* **62** 086028
[18] Joffrin E. *et al* 2019 *Nucl. Fusion* **59** 112021
[19] Parisi J.F. *et al* 2022 *Nucl. Fusion* **62** 086045
[20] Field A.R., Chapman-Oplopoiou B., Connor J.W., Frassinetti L., Hatch D.R., Roach C.M. and Saarelma S. (JET Contributors) 2023 *Phil. Trans. R. Soc.* A **381** 20210228

[21] Told D. 2012 Gyrokinetic microturbulence in transport barriers *PhD Thesis* Universität Ulm
[22] Dickinson D., Roach C.M., Saarelma S., Scannell R., Kirk A. and Wilson H.R. 2012 *Phys. Rev. Lett.* **108** 135002
[23] Dickinson D., Roach C.M., Saarelma S., Scannell R., Kirk A. and Wilson H.R. 2013 *Plasma Phys. Control. Fusion* **55** 074006
[24] Hatch D.R., Kotschenreuther M., Mahajan S., Valanju P., Jenko F., Told D., Görler T. and Saarelma S. 2016 *Nucl. Fusion* **56** 104003
[25] Pueschel M.J., Hatch D.R., Kotschenreuther M., Ishizawa A. and Merlo G. 2020 *Nucl. Fusion* **60** 124005
[26] Hassan E., Hatch D.R., Halfmoon M.R., Curie M., Kotchenreuther M.T., Mahajan S.M., Merlo G., Groebner R.J., Nelson A.O. and Diallo A. 2022 *Nucl. Fusion* **62** 026008
[27] Chen L., Zonca F. and Lin Z. 2005 *Plasma Phys. Control. Fusion* **47** B71
[28] Lin Z., Chen L. and Zonca F. 2005 *Phys. Plasmas* **12** 056125
[29] Kotschenreuther M., Liu X., Mahajan S.M., Hatch D.R. and Merlo G., *Regimes of Weak ITG/TEM Modes for Transport Barriers Without Velocity Shear, and a Statistical Mechanical Ansatz* (Institution for Fusion Studies, The University of Texas at Austin)
[30] Parisi J.F. *et al* 2020 *Nucl. Fusion* **60** 126045
[31] Landreman M. and Ernst D.R. 2012 *Plasma Phys. Control. Fusion* **54** 115006
[32] Candy J., Belli E.A. and Staebler G. 2020 *Plasma Phys. Control. Fusion* **62** 042001
[33] Parra1 F. and Barnes M. 2015 *Plasma Phys. Control. Fusion* **57** 054003
[34] Mahajan S.M. and Krishan V. 2008 *Astrophys. J.* **682** 602
[35] Pueschel M.J., Jenko F., Told D. and Büchner J. 2011 *Phys. Plasmas* **18** 112102
[36] Hatch D.R. 2010 Mode analyses of gyrokinetic simulations of plasma microturbulence *PhD Thesis* University of Wisconsin-Madison
[37] Walker J. and Hatch D.R. 2023 *Phys. Plasmas* **30** 082307
[38] Arakawa A. 1966 *J. Comput. Phys.* **1** 119